GEOPHYSICS, VOL. 84, NO. 4 (JULY-AUGUST 2019); P. WA141–WA151, 9 FIGS., 3 TABLES.
10.1190/GEO2018-0487.1

Modeling wave propagation in cracked porous media with penny-shaped inclusions

Lin Zhang[1], Jing Ba[1], José M. Carcione[2], and Weitao Sun[3]

ABSTRACT

Understanding acoustic wave dispersion and attenuation induced by local (squirt) fluid flow between pores and cracks (compliant pores) is fundamental for better characterization of the porous rocks. To describe this phenomenon, some squirt-flow models have been developed based on the conservation of the fluid mass in the fluid mechanics. By assuming that the cracks are represented by isotropically distributed (i.e., randomly oriented) penny-shaped inclusions, this study applies the periodically oscillating squirt flow through inclusions based on the Biot-Rayleigh theory, so that the local squirt flow and global wave oscillation of rock are analyzed in the same theoretical framework of Hamilton's principle. The governing wave-propagation equations are derived by incorporating all of the crack characteristics (such as the crack radius, crack density, and aspect ratio). In comparison with the previous squirt models, our model predicts the similar characteristics of wave velocity dispersion and attenuation, and our results are in agreement with Gassmann equations at the low-frequency limit. In addition, we find that the fluid viscosity and crack radius only affect the relaxation frequency of the squirt-flow attenuation peak, whereas the crack density and aspect ratio also affect the magnitudes of dispersion and attenuation. The application of this study to experimental data demonstrates that when the differential pressure (the difference between confining pressure and pore pressure) increases, the closure of cracks can lead to a decrease of attenuation. The results confirm that our model can be used to analyze and interpret the observed wave dispersion and attenuation of real rocks.

INTRODUCTION

It is commonly accepted that the presence of cracks in subsurface rocks plays an important role in seismic wave propagation. Cracks mostly refer to grain contacts or intragranular microfractures (Gurevich et al., 2009a), with a size of 10^{-5}–10^{-2}, which not only affect the elastic properties of the fractured porous rock but also control the local fluid flow (LFF) between cracks and stiff pores, often called the squirt-flow mechanism (e.g., Müller et al., 2010; Carcione, 2014). Especially, this flow mechanism is the main contributor of wave dispersion and attenuation, which are highly affected by the lithology, pore structure, and fluid properties (e.g., Quintal et al., 2011; Yao et al., 2015; Khalid and Ahmed, 2016). Therefore, knowledge about the dispersion and attenuation dependence on fluid flow is important in seismic interpretation and reservoir characterization.

Many effective medium theories (e.g., Eshelby, 1957; Walsh, 1965; Mori and Tanaka, 1973; Kuster and Toksöz, 1974; Berryman, 1980; Norris, 1985; Thomsen, 1985; Song et al., 2016) and laboratory experiments (e.g., Fortin et al., 2007; Adam and Otheim, 2013; Wang et al., 2018; Yin et al., 2018) have been proposed to investigate the effects of cracks on the elastic properties of rocks. For example, using Eshelby's tensor, David and Zimmerman (2011) calculate the elastic moduli of an isotropic solid containing a random distribution and random orientation of spheroidal pores. Although cracks represent an extremely small volume fraction (often less than 0.1%), their effects are important. Without considering the shape of the cracks, Shapiro (2003) provides analytical expressions for the elastic moduli of a cracked porous medium as a function of pressure, stiff porosity ϕ_s, and compliant porosity ϕ_c. Because the crack features

Manuscript received by the Editor 27 June 2018; revised manuscript received 9 February 2019; published ahead of production 4 April 2019; published online 31 May 2019.
[1]Hohai University, School of Earth Sciences and Engineering, Nanjing 211100, China. E-mail: zlin@hhu.edu.cn; baj04@mails.tsinghua.edu.cn; jba@hhu.edu.cn (corresponding author).
[2]Istituto Nazionale di Oceanografia e di Geofisica Sperimentale (OGS), Borgo Grotta Gigante 42c, Sgonico, Trieste I-34010, Italy. E-mail: jcarcione@inogs.it.
[3]Tsinghua University, Zhou Pei-Yuan Center for Applied Mathematics, Beijing 100084, China. E-mail: sunwt@tsinghua.edu.cn.

are closely related to pressure variations, some researchers estimate the pore aspect-ratio distribution from the pressure dependence of dry velocities based on different theories (e.g., Cheng and Toksöz, 1979; Tran et al., 2008; David and Zimmerman, 2012). Although such methods can provide the crack characteristics, they do not describe the observed values of velocity dispersion and attenuation, which is due to the fact that there is no fluid exchange between the cracks and the porous background.

Classic approaches to handle this problem are mostly based on Biot's poroelastic theory, which considers the global-flow mechanism in saturated porous media (Biot, 1956, 1962) and is equivalent to Gassmann (1951) in the low-frequency limit. However, it is not suitable to model the fluid flow between pores and cracks. Hence, several models have been proposed in the past few decades to address this local mechanism (e.g., Mavko and Nur, 1975; Murphy et al., 1986; Gurevich et al., 2009b). Nevertheless, both flow mechanisms coexist in a cracked porous medium. The squirt-flow Biot/squirt model theory has been developed by Dvorkin and Nur (1993), but the crack characteristics are not taken into account. Tang (2011) and Tang et al. (2012) add crack density and aspect ratio into their model, referred to here as the Tang model, and they find that the relaxation frequency and the amount of wave dispersion and attenuation are controlled by the crack aspect ratio and density, respectively. However, these squirt-flow models are not compatible with Gassmann's theory. Models consistent with Gassmann's theory include Berryman and Wang (1995), Pride and Berryman (2003), Gurevich et al. (2010), Carcione and Gurevich (2011), Ba et al. (2016), and Zheng et al. (2017). In Chapman et al. (2002), a microstructural model is derived, which is consistent with the Gassmann's theory and the results of Endres and Knight (1997), hereafter referred to as the Chapman model. Pride et al. (2004) propose that the cracks can be treated as penny-shaped inclusions. Yao et al. (2015) add a flow term induced by the squirt flow into the original fluid modulus and modeled wave dispersion and attenuation by using the dynamic fluid modulus (the so-called DFM model).

Anisotropy caused by the presence of cracks was considered by Hudson et al. (1996), Chapman (2003), and Guo et al. (2018a, 2018b). Jakobsen et al. (2003) study the effects of pores and cracks on the elastic behavior by considering an arbitrary distribution of pores and fractures using the T-matrix approach. An alternative scheme based on the solutions of a single-crack and multiple-scattering theory is that of Galvin and Gurevich (2009). They analyze the elastic wave dispersion and attenuation in a porous medium containing aligned sparsely distributed penny-shaped cracks. Furthermore, Guo et al. (2017) investigate the relations between the elastic properties of rocks with intersecting fractures.

The purpose of this study is to model the fluid flow between the background pores and cracks, in which these can be treated as penny-shaped inclusions. Here, we assume that all of the cracks are isotropically distributed. The fluid-flow mechanism is based on the Biot-Rayleigh theory, which describes the fluid flow between two pore volumes using periodic oscillations (Ba et al., 2011, 2017). We derive the LFF governing equations from the above assumption and verify the effectiveness of the new model by comparison with the Biot, Chapman, Tang, and DFM models, and we analyze the effects of fluid viscosity and crack characteristics on wave propagation. Finally, the model results are compared with measurements on two tight sandstones.

WAVE-PROPAGATION EQUATIONS

Let us consider that cracks with different aspect ratios are randomly oriented distributed in the pore space (see Figure 1a) and fluid flows between cracks and pores. Here, cracks are described as penny-shaped inclusions into a host medium saturated with the same fluid (see Figure 1b). Similar to the Biot-Rayleigh theory, the cracked porous model is based on the following assumptions (Ba et al., 2011): (1) The penny-shaped inclusions are homogeneous and have the same radius R_0 and height h; hence, the aspect ratio ($\gamma = h/(2R_0)$) of all the cracks is the same. (2) The size of the inclusions is much smaller than the wavelength, so that the cracks are in an isostress state, and we consider a unit cell as shown in Figure 1b. (3) The fluid flow between an inclusion and the host medium takes place mainly along the radial direction (see Figure 1c) because for a single crack in the model, the permeability in the radial direction is much higher than that along the axis (can be infinitesimal in the approximation; for a similar model, see Gurevich et al., 2010). (4) The fraction of inclusions is small.

Stress-strain relations

A cracked porous medium has been widely described by using the double-porosity model (e.g., Berryman and Wang, 1995; Ba et al., 2016; Zheng et al., 2017). As in Ba et al. (2011), the strain energy can be defined as

$$2W = (\lambda_c + 2\mu)e^2 - 4\mu I_2 - 2\alpha_1 M_1 e(\xi^{(1)} - \phi_1\phi_2\varsigma) - 2\alpha_2 M_2 e(\xi^{(2)} + \phi_1\phi_2\varsigma) + M_1(\xi^{(1)} - \phi_1\phi_2\varsigma)^2 + M_2(\xi^{(2)} + \phi_1\phi_2\varsigma)^2, \quad (1)$$

where $e_{ij} = 1/2(\partial_j u_i + \partial_i u_j)$ are the solid strain components and $e = \nabla \cdot \mathbf{u}$; $\xi^{(m)} = -\nabla \cdot \mathbf{w}^{(m)}$ is the increment of fluid content (m = 1, 2 represent the host medium and inclusions, respectively); $\mathbf{w}^{(m)} = \phi_m(\mathbf{U}^{(m)} - \mathbf{u})$, where $\mathbf{U}$ and $\mathbf{u}$ are the fluid and solid displacements, respectively; I_2 is the second invariant of the solid strain; ϕ is the total porosity, which is defined as $\phi = \phi_1 + \phi_2$,where ϕ_1 and ϕ_2 are the porosities of the host medium and inclusions, respectively, with $\phi_m = v_m\Phi_{m0}$, where v_m and Φ_{m0} are the volume fraction of the m phase and the matrix porosity of a local area internal to the m phase; μ is the shear modulus of the rock (composite); and λ_c, α_1, α_2, M_1, and M_2 are the stiffness coefficients (see Appendix A). Due

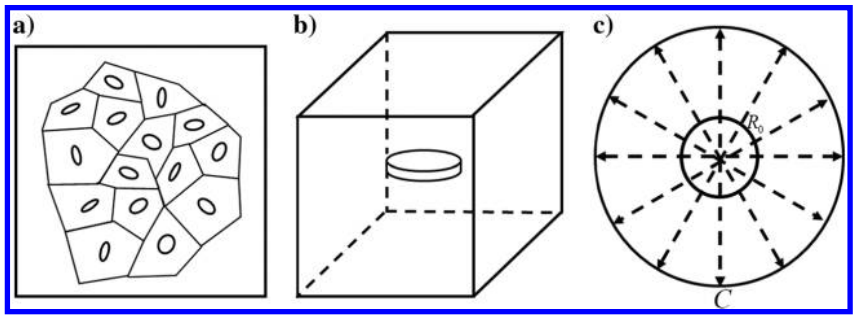

Figure 1. Scheme of the cracked porous model. (a) Distribution of cracks with different aspect ratios, (b) penny-shaped inclusion, and (c) fluid flow between inclusions and the host medium occurs along the radial direction.

to the flow mechanism, described by periodic cylindrical oscillations, the fluid variation ς between the host medium and the penny-shaped inclusions is given by

$$\varsigma = \frac{1}{\phi_1}\left(1 - \frac{R_0^2}{R^2}\right), \tag{2}$$

where R is the dynamic radius of the inclusion after wave-induced LFF.

From the energy (equation 1), the stress-strain relations are given by

$$\tau_{ij} = 2\mu e_{ij} + (\lambda_c e - \alpha_1 M_1(\xi^{(1)} - \phi_1\phi_2\varsigma) - \alpha_2 M_2(\xi^{(2)} + \phi_1\phi_2\varsigma))\delta_{ij}, \tag{3a}$$

$$P_{f1} = -\alpha_1 M_1 e + M_1(\xi^{(1)} - \phi_1\phi_2\varsigma), \tag{3b}$$

$$P_{f2} = -\alpha_2 M_2 e + M_2(\xi^{(2)} + \phi_1\phi_2\varsigma), \tag{3c}$$

where δ_{ij} is the Kronecker delta (i and j are the three Cartesian coordinates x, y, and z), τ_{ij} is the total stress, and P_{fm} are the pore-fluid pressures in each phase.

Equations of motion

The equations of motion are based on Biot (1962) and Ba et al. (2011):

$$\tau_{ij,j} = \rho\ddot{u}_i + \rho_f\ddot{w}_i^{(1)} + \rho_f\ddot{w}_i^{(2)}, \tag{4a}$$

$$(-P_{f1})_{,i} = \rho_f\ddot{u}_i + m_1\dot{w}_i^{(1)} + \frac{\eta}{\kappa_1}\frac{\phi_{10}}{\phi_1}\dot{w}_i^{(1)}, \tag{4b}$$

$$(-P_{f2})_{,i} = \rho_f\ddot{u}_i + m_2\dot{w}_i^{(2)} + \frac{\eta}{\kappa_2}\frac{\phi_{20}}{\phi_2}\dot{w}_i^{(2)}, \tag{4c}$$

where the comma preceding an index indicates the partial spatial differentiation, the dot above a variable denotes a partial time derivative, η is the fluid viscosity, κ_1 and κ_2 are the permeabilities of the host medium and inclusions, respectively, ρ and ρ_f are the densities of the porous aggregate and pore fluid, where $\rho = (1-\phi)\rho_s + \phi\rho_f$, where ρ_s is the grain density, and the coefficients m_1 and m_2 are defined as (Biot, 1962)

$$m_1 = \frac{\tau_1\rho_f}{\phi_1}, \qquad m_2 = \frac{\tau_2\rho_f}{\phi_2}, \tag{5}$$

where τ_1 and τ_2 represent the tortuosities of the host medium and inclusions, respectively.

The LFF governing equation

As in the Biot-Rayleigh theory (Ba et al., 2011), the fluid flow between the host medium and a penny-shaped inclusion can be modeled by periodic cylindrical oscillations. Hence, the kinetic and dissipation functions are also derived with a generalization of the Rayleigh theory (Rayleigh, 1917) and the Biot poroelastic theory (Biot, 1962). First, the kinetic energy function T is determined by

$$T = \frac{1}{2}\rho\sum_i \dot{u}_i^2 + \frac{1}{2}m_1\sum_i(\dot{w}_i^{(1)})^2 + \frac{1}{2}m_2\sum_i(\dot{w}_i^{(2)})^2 + \rho_f\dot{u}_i\dot{w}_i^{(1)} + \rho_f\dot{u}_i\dot{w}_i^{(2)} + T_{\mathrm{LFF}}, \tag{6}$$

where

$$T_{\mathrm{LFF}} = \frac{3}{16}\rho_f\phi_1^2\phi_2 R_0^2\dot{\varsigma}^2 + \frac{1}{4}\rho_f\frac{\phi_1^2\phi_2\phi_{20}}{\phi_{10}}\ln\frac{L+R_0}{R_0}R_0^2\dot{\varsigma}^2 \tag{7}$$

is the kinetic energy function induced by the LFF in the inclusions and host medium (see Appendix B) and L is the characteristic fluid flow length $L = (R_0^2/12)^{1/2}$ (Pride et al., 2004).

Table 1. Input properties: K_s, μ_s, and ρ_s are the bulk modulus, shear modulus, and density of the solid grains; K_f, ρ_f, and η are the bulk modulus, density, and viscosity of the fluid; ϕ_{10}, κ_1, c_1, and τ_1 are the matrix porosity, permeability, consolidation parameter, and tortuosity of the host medium; ϕ_{20}, κ_2, and τ_2 are the matrix porosity, permeability, and tortuosity of the inclusions; and ε, γ, and R_0 are the crack density, aspect ratio, and crack radius.

Property	Figure 2	Figure 3	Figure 4	Figure 5	Figure 6
K_s (GPa)	37.9[a]	21.83[b]	37.9[a]	37.9[a]	37.9[a]
μ_s (GPa)	32.6[a]	24.5[b]	32.6[a]	32.6[a]	32.6[a]
ρ_s (kg/m^3)	2650[a]	2637.8[b]	2650[a]	2650[a]	2650[a]
K_f (GPa)	2.25[a]	2.9[b]	2.25[a]	2.25[a]	2.25[a]
ρ_f (kg/m^3)	1000[a]	1097[b]	1000[a]	1000[a]	1000[a]
η (Pa·s)	0.001[a]	0.001[b]	0.01	0.01	0.001, 0.01, 0.1
ϕ_{10}	0.25[a]	0.227[b]	0.25[a]	0.25[a]	0.25[a]
ϕ_{20}	0.32[c]	0.32[c]	0.32[c]	0.32[c]	0.32[c]
κ_1 (D)	0.1[a]	0.2	0.1[a]	0.1[a]	0.1[a]
κ_2 (D)	100	200	100	100	100
c_1	11	—	11	11	11
τ_1	2.4[a]	2.7026	2.4[a]	2.4[a]	2.4[a]
τ_2	1	2.0625	1	1	1
ε	0.2[a]	0.0146	0.2[a]	0.16, 0.18, 0.2	0.2[a]
γ	0.002[a]	0.0001	0.002[a]	0.0001, 0.0005, 0.0018, 0.002	0.002[a]
R_0 (m)	0.0053	0.0001	Variable	0.01	0.0053

[a]From Tang et al. (2012).
[b]From Chapman (2001).
[c]From Pride et al. (2004).

In a similar way, the dissipation function D is given by

$$D = \frac{1}{2}\phi_1\phi_{10}\left(\frac{\eta}{\kappa_1}\right)\dot{w}_i^{(1)} \cdot \dot{w}_i^{(1)} + \frac{1}{2}\phi_2\phi_{20}\left(\frac{\eta}{\kappa_2}\right)\dot{w}_i^{(2)} \cdot \dot{w}_i^{(2)} + D_{\mathrm{LFF}}, \tag{8}$$

where

$$D_{\mathrm{LFF}} = \frac{3}{16}\frac{\eta\phi_1^2\phi_{20}\phi_2}{\kappa_2}R_0^2\dot{\varsigma}^2 + \frac{1}{4}\frac{\eta\phi_1^2\phi_{20}\phi_2}{\kappa_1}\ln\frac{L+R_0}{R_0}R_0^2\dot{\varsigma}^2 \tag{9}$$

is the dissipation energy function induced by the LFF in the inclusions and host medium (see Appendix B).

Following Achenbach (1984), the Lagrange equation is

$$\frac{d}{dt}\left(\frac{\partial L_e}{\partial\dot{\varsigma}}\right) + \frac{\partial L_e}{\partial\varsigma} + \frac{\partial D}{\partial\dot{\varsigma}} = 0, \tag{10}$$

where $L_e = T - W$.

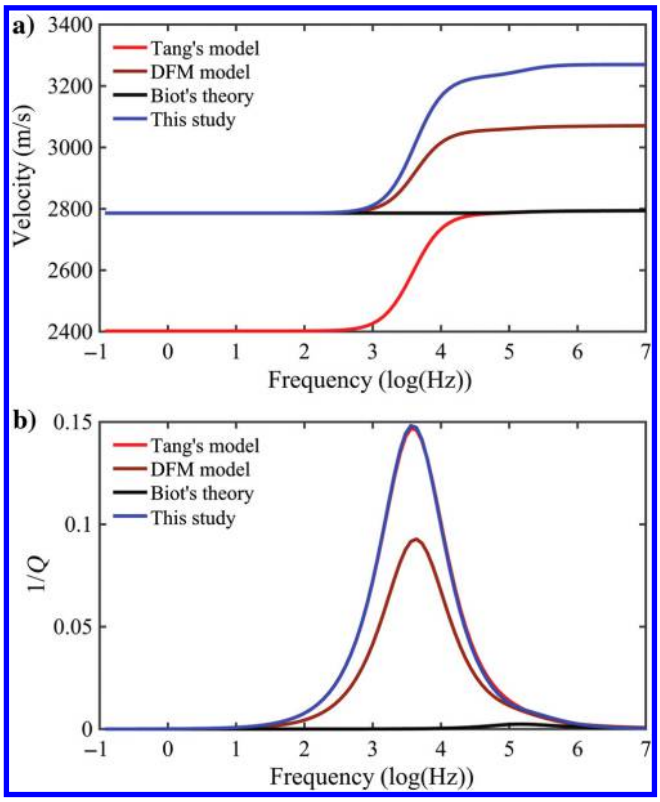

Figure 2. (a) The P-wave dispersion and (b) attenuation using the rock and fluid properties listed in Table 1. The solid red, solid black, solid brown, and solid blue curves represent the results of Biot's theory, Tang's model, DFM model, and this study, respectively.

Finally, the LFF governing equation is

$$\left(\frac{3}{8} + \frac{\phi_{20}}{2\phi_{10}}\ln\frac{L+R_0}{R_0}\right)\phi_1^2\phi_2\rho_f R_0^2\ddot{\varsigma} + \left(\frac{3\eta}{8\kappa_2} + \frac{\eta}{2\kappa_1}\ln\frac{L+R_0}{R_0}\right) \times \phi_{20}\phi_1^2\phi_2 R_0^2\dot{\varsigma} = \phi_1\phi_2(\alpha_1 M_1 - \alpha_2 M_2) e + \phi_1\phi_2(M_2\xi^{(2)} - M_1\xi^{(1)}) + \phi_1^2\phi_2^2(M_1 + M_2)\varsigma. \tag{11}$$

Plane-wave analysis

From equations 3, 4, and 11, we can finally obtain the equations of motion. These equations are written in the form of plane-wave solutions:

$$(u_i, \dot{w}_i^{(1)}, \dot{w}_i^{(2)}, \varsigma) = (A, B_1, B_2, C)e^{i(\omega t - k\cdot\mathbf{x})}, \tag{12}$$

where (A, B_1, B_2, C) define the polarizations of the solid, the fluid flow in two pore volumes and the LFF, ω is the angular frequency, and k is the complex wavenumber. Thus, the complex velocity can be determined by

$$v = \frac{\omega}{k}, \tag{13}$$

and the P-wave velocities are

$$V_{\mathrm{P}} = \left(\mathrm{Re}\left(\frac{1}{v}\right)\right)^{-1}. \tag{14}$$

In addition, the quality factor is defined as

$$Q = \frac{\mathrm{Re}(k)}{2\mathrm{Im}(k)}, \tag{15}$$

where $\omega = 2\pi f$, with the frequency f (e.g., Carcione, 2014).

RESULTS

In this section, we analyze the effect of cracks on the elastic wave attenuation and velocity dispersion. Table 1 gives a list of the rock and fluid properties. The porosity of cracks can be expressed as $\phi_c = 2\pi\epsilon\gamma$, where $\phi_2 = \phi_c$ and ϵ is the crack density (Tang, 2011). The dry-rock moduli of the composite can be calculated by using a Biot-consistent theory (Thomsen, 1985) as follows:

$$K_b = \frac{2}{3}\frac{(1+v_B)}{(1-2v_B)}\mu_b \tag{16}$$

and

$$\mu_b = \mu_s\left(1 - \frac{\phi}{1-b_B} - B_B\varepsilon\right), \tag{17}$$

where $b_B = (2/15)((4-5v_B)/(1-v_B))$, $B_B = (32/45)((1-v_B)(5-v_B)/(2-v_B))$, μ_s is the shear modulus of the solid grains, and v_B is the Poisson's ratio. The dry bulk modulus of the host medium is given by (Pride et al., 2004)

$$K_{b1} = \frac{(1-\phi_{10})K_s}{1+c_1\phi_{10}}, \tag{18}$$

where c_1 is the consolidation parameter of the host medium (it represents the degree of consolidation between the grains; see Pride et al., 2004) and the dry modulus of the inclusion is obtained from $v_2/K_{b2} = 1/K_b - v_1/K_{b1}$.

Comparison to other models

Figure 2 compares the Tang model (Tang et al., 2012), the DFM model (Yao et al., 2015), and ours, using the rock and fluid properties in Table 1, which are those of Tang et al. (2012). The P-wave velocities of the present model and the DFM model are in good agreement with Biot's curve at low frequencies (the velocity of Biot's theory approaches that of Gassmann's [1951] theory at low frequencies) (i.e., below 10^4 Hz, Dunn, 1986), whereas the results of the Tang model are in agreement with Biot's curve at high frequencies (approximately 10^5 Hz, Tang et al., 2012). This is because the squirt flow of the Tang model is described by using the conservation of the fluid mass, and the additional fluid content change due to the squirt flow into pore space is q_v. The pore pressure in turn will be changed due to the fluid content variation ϕq_v. Tang et al. (2012) use $S(\omega) = \phi q_v/p$ to characterize the squirt flow effect on the pore pressure p. Hence, the contribution of squirt flow to the saturated bulk modulus is related to $S(\omega)$ (see equations C-1 and C-2). At low frequencies, $S(\omega)$ has a finite nonzero value (Tang's model gives a low-frequency limit below the Gassmann's theory), whereas it is zero at high frequencies.

We describe the oscillating squirt flow through penny-shaped inclusions based on the Biot-Rayleigh theory, which is derived from Hamilton's principle. We derive the elastic coefficients such that they are consistent with Gassmann's theory at the low-frequency limit, such as for the DFM model (Yao et al., 2015). The rock is fully relaxed at low frequencies, and the bulk modulus increases to an unrelaxed value at the high-frequency limit. Moreover, the magnitude of attenuation predicted by our model is almost the same as that by the model of Tang (2011) and Tang et al. (2012), with higher values compared to the DFM model in the frequency range of $10^1 - 10^5$ Hz.

A comparison between the Chapman model and our model is given in Figure 3, with the properties given in Table 1 (Chapman, 2001). The dry-rock moduli of the composite are estimated from the velocities of the saturated rock by using Gassmann's theory. The fitting parameters are the dry-rock moduli of the composite, $K_b = 14.626$ GPa, and $\mu_b = 12.539$ GPa . For both theoretical models, the P-wave velocities increase with the increasing frequency. The velocity curves predicted by the models are consistent with the Gassmann limit at low frequencies. Differences between the Chapman model and our model occur at high frequencies. The crack density is the only parameter that controls the magnitude of the velocity dispersion curve in the Chapman model (Chapman et al., 2002), whereas this dispersion is dependent on the crack density ε and crack aspect ratio γ in our study.

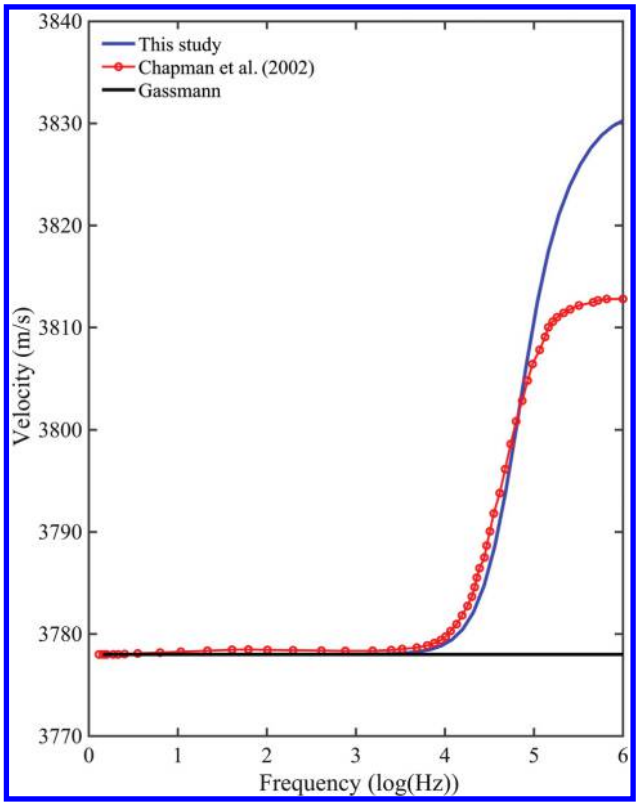

Figure 3. The P-wave velocity as a function of frequency. The solid blue, solid red, and solid black curves represent the results of this study, Chapman model, and Gassmann's theory, respectively.

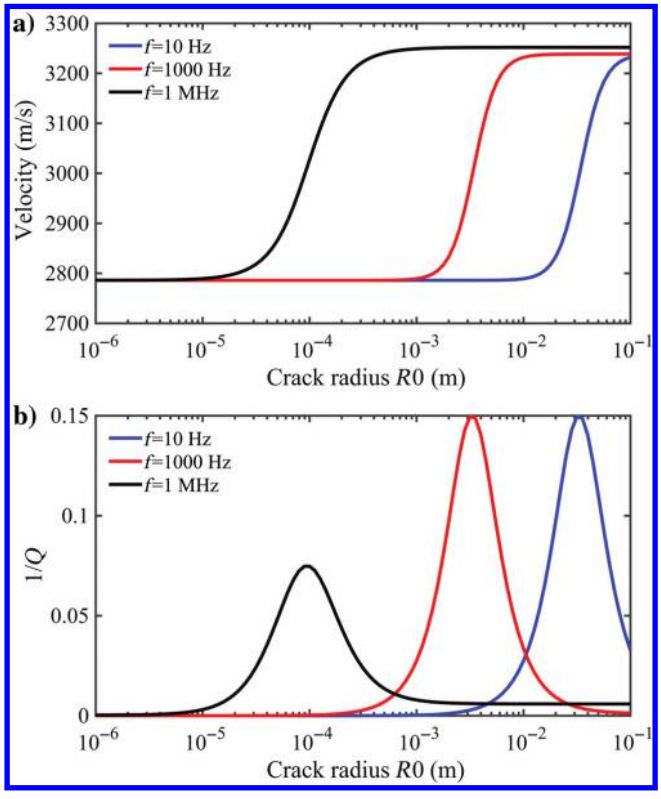

Figure 4. (a) The P-wave dispersion and (b) attenuation as a function of crack radius, using the rock and fluid properties listed in Table 1. The solid blue, solid red, and solid black curves correspond to $f = 10$ Hz, 1 kHz, and 1 MHz, respectively.

According to the above analysis, we have introduced the effects of the LFF between the cracks and the pores, and the predictions are consistent with the Biot-Gassmann theory.

Wave dispersion and attenuation analysis

Figure 4 shows the P-wave dispersion (Figure 4a) and attenuation (Figure 4b) as a function of the crack radius R_0. The values 10 Hz, 1 kHz, and 1 MHz represent the seismic, log, and ultrasonic frequencies, respectively. When the crack porosity is constant, the P-wave velocity increases with increasing crack radius, approaching a constant value. In addition, the attenuation is due to the combined effect of the global and squirt flows at the ultrasonic frequency band. The attenuation curve controlled by the squirt flow moves toward low frequencies with increasing crack radius. The results show that the crack radius controls the relaxation frequency of the squirt flow.

Figure 5 shows the P-wave dispersion (Figure 5a) and attenuation (Figure 5b) for different crack density ε and aspect ratio γ: $\varepsilon = 0.16$, $\gamma = 0.002$; $\varepsilon = 0.18$, $\gamma = 0.002$; $\varepsilon = 0.2$, $\gamma = 0.002$; $\varepsilon = 0.2$, $\gamma = 0.0018$; $\varepsilon = 0.2$, $\gamma = 0.0005$; and $\varepsilon = 0.2$, $\gamma = 0.0001$. The results indicate that keeping constant the crack aspect ratio, the larger the crack density, the larger the amount of attenuation and dispersion caused by the squirt flow. In contrast, when the crack density is constant, the larger the crack aspect ratio, the smaller the levels of attenuation and dispersion. Then, at high frequencies, the dispersion and attenuation induced by the global flow (Biot's theory) are the same for all of the crack porosities. This is because the crack porosity is much smaller than the porosity of the host medium and the global flow is mainly affected by the properties of the host medium. Moreover, the P-wave velocity and attenuation curves controlled by the squirt flow extend to the low frequencies with the increasing crack density and decreasing crack aspect ratio. Regarding the effects of the crack density and aspect ratio on the P-wave velocity and attenuation, two conclusions are highlighted: crack density is the main factor affecting the amount of dispersion and attenuation induced by the squirt flow (Figure 5; see the solid blue, solid red, and solid black curves, respectively), whereas the crack aspect ratio mainly affects the relaxation frequency of the squirt flow (Figure 5; see the solid magenta, solid green, and solid brown curves, respectively). Similar conclusions can be found in other works (e.g., Berryman, 2007; Tang et al., 2012). It can also be noted that when the media have the same crack porosity (Figure 5; see the solid magenta and solid red curves, respectively), the variation of the crack density and aspect ratio can cause a significant difference of P-wave velocity and attenuation, which highlights that knowledge of the pore geometry is essential to adequately predict these properties.

The P-wave dispersion and attenuation at different fluid viscosities are given in Figure 6. With the increasing fluid viscosity, the relaxation frequency of the squirt and global flows shift to the low and high frequencies, respectively (see Ba et al., 2011). The fluid viscosity only affects the P-wave relaxation frequency, with no effect on the magnitude of the wave velocity at the low- and high-frequency limits.

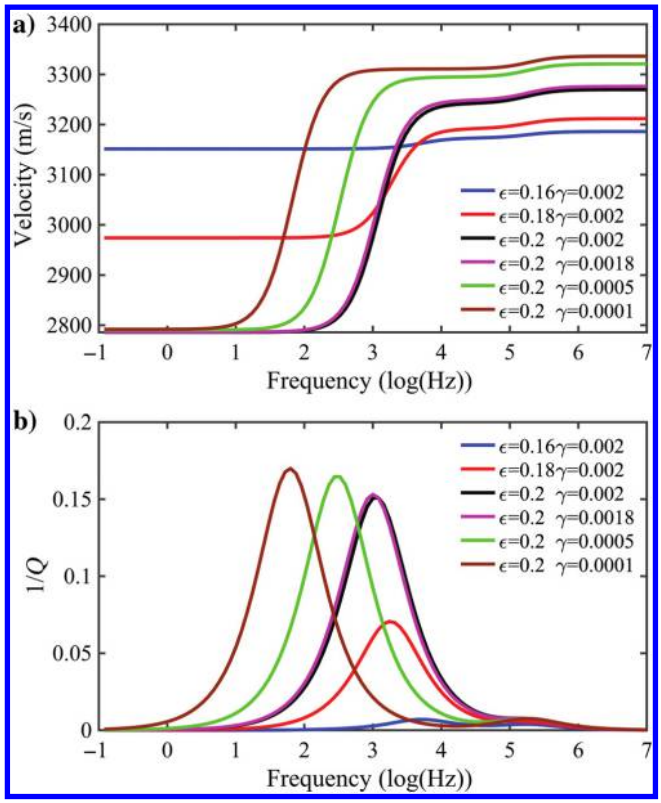

Figure 5. (a) The P-wave dispersion and (b) attenuation with different crack density ε and aspect ratio γ, using the rock and fluid properties listed in Table 1. The solid blue, solid red, solid black, solid magenta, solid green, and solid brown curves correspond to $\varepsilon = 0.16$, $\gamma = 0.002$; $\varepsilon = 0.18$, $\gamma = 0.002$; $\varepsilon = 0.2$, $\gamma = 0.002$; $\varepsilon = 0.2$, $\gamma = 0.0018$; $\varepsilon = 0.2$, $\gamma = 0.0005$; and $\varepsilon = 0.2$, $\gamma = 0.0001$, respectively.

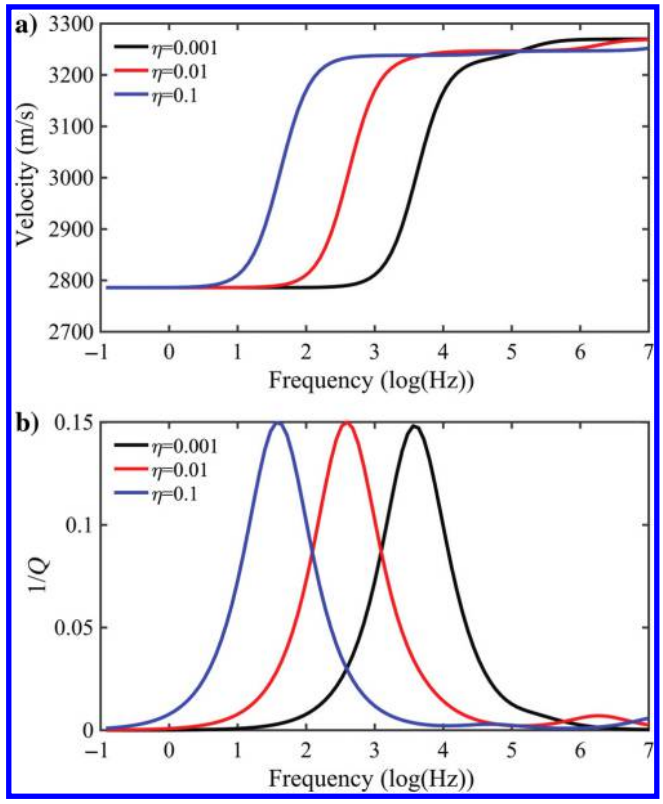

Figure 6. (a) The P-wave dispersion and (b) attenuation at different fluid viscosities, based on the rock and fluid properties given in Table 1. The solid blue, solid red, and solid black curves correspond to $\eta = 0.1$, 0.01, and 0.001, respectively.

COMPARISON TO EXPERIMENTAL DATA

Here, we model the pressure dependence of the wave velocity at full saturation. We assume that the pore structure of a rock saturated with a fluid remains the same as in the dry test and that the pore aspect ratio distribution can be estimated from the pressure dependence of the dry velocities. Figure 7 shows the P- and S-wave velocities as a function of the differential pressure for two dry tight sandstone samples. These samples are from southwest of the Sichuan Basin and are composed of quartz, feldspar, debris, and mica, etc. The experiments are performed at a frequency of 1 MHz, a temperature of 80°C, and a varying differential pressure of 5–35 MPa. The rock properties of the samples are listed in Table 2. The experimental setup can be found in Ba et al. (2018). The pore fluid used in the experiments is water, whose bulk modulus, density, and viscosity are 2.41 GPa, 1010kg/m^3, and 0.000938 Pa·s, respectively. In Figure 7, we can see the nonlinear features of the pressure-velocity curve, which implies that the cracks close with increasing differential pressure. In addition, the predictions of the Mori-Tanaka model (e.g., Mori and Tanaka, 1973) for two rock samples are all in good agreement with the measurements.

Table 2. Properties of the rock samples

Tight sandstone	K_s (GPa)	μ_s (GPa)	ρ_s (kg/m^3)	ϕ_{10} (%)	κ_1 (mD)	R_0 (m)
1	39	33	2672	6.26	0.046	0.000005
2	39	35	2660	13.91	1.37	0.000035

David and Zimmerman (2012) develop a procedure for calculating the pore aspect ratio distribution, according to the Mori-Tanaka model (e.g., Mori and Tanaka, 1973). According to this procedure, the aspect ratio γ of the stiff porosity for tight sandstone samples 1 and 2 is 0.05 and 0.07, respectively. Figure 8 displays the crack porosity ϕ_c (Figure 8a) and density ε (Figure 8b) as a function of pressure for the two rock samples. The crack porosity and density decrease with pressure p, and all cracks are almost closed at high pressure. The crack porosity and density are used to estimate the saturated velocities.

The dry-rock moduli of the samples can be estimated from dry measurements by using the Mori-Tanaka model. The dry-rock bulk modulus of the host medium is given in equation 16, and the consolidation c_1 is a fitting parameter whose value decreases with increasing differential pressure. For sample 1, the values of c_1 at each pressure are 6.4, 5.6, 5.2, 4.7, 4, 3.4, and 3.4; for sample 2, the values are 11.2, 9, 7.6, 6.8, 6.4, 6, and 5.7. In addition, we assume that the crack radius R_0 is constant for different differential pressures. Figure 9 shows the P-wave velocities of the water-saturated tight sandstone samples. Based on the Mori-Tanaka model, the dry bulk and shear moduli for the rock samples can be obtained and the saturated velocities can be calculated with the Gassmann equation. The results from Gassmann equation are lower than the measurements,

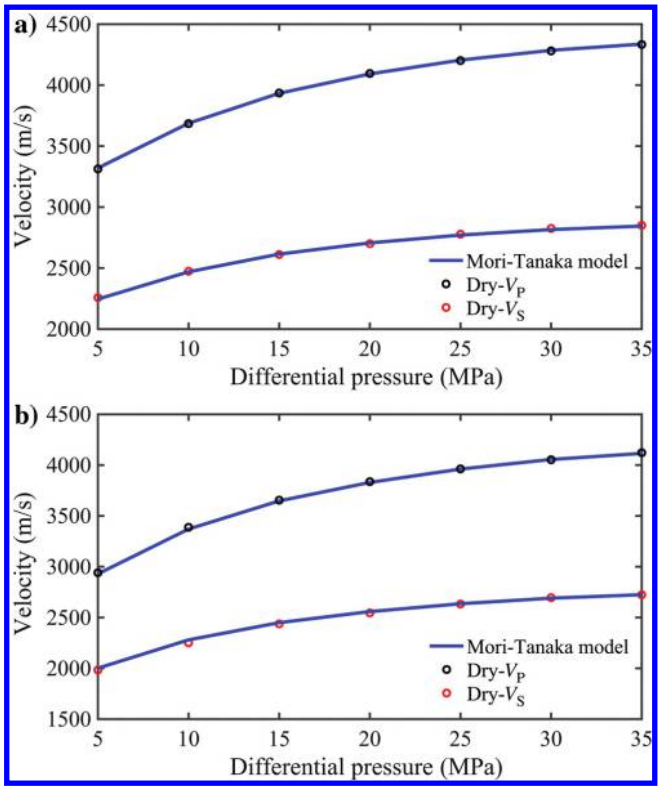

Figure 7. The P- and S-wave velocities as a function of the differential pressure for the tight sandstone samples (a) 1 and (b) 2. The blue line is the predicted results of the Mori-Tanaka model, and the circles are measurements.

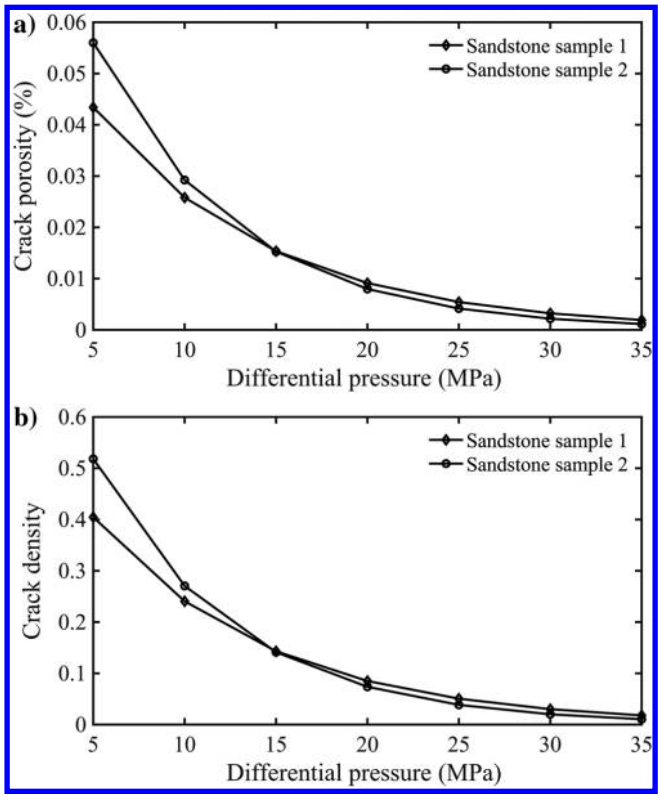

Figure 8. (a) Crack porosity and (b) density as a function of the differential pressure for the two tight sandstone samples, according to David and Zimmerman (2012) model. The solid curves with circles and diamonds correspond to the tight sandstone samples 1 and 2, respectively.

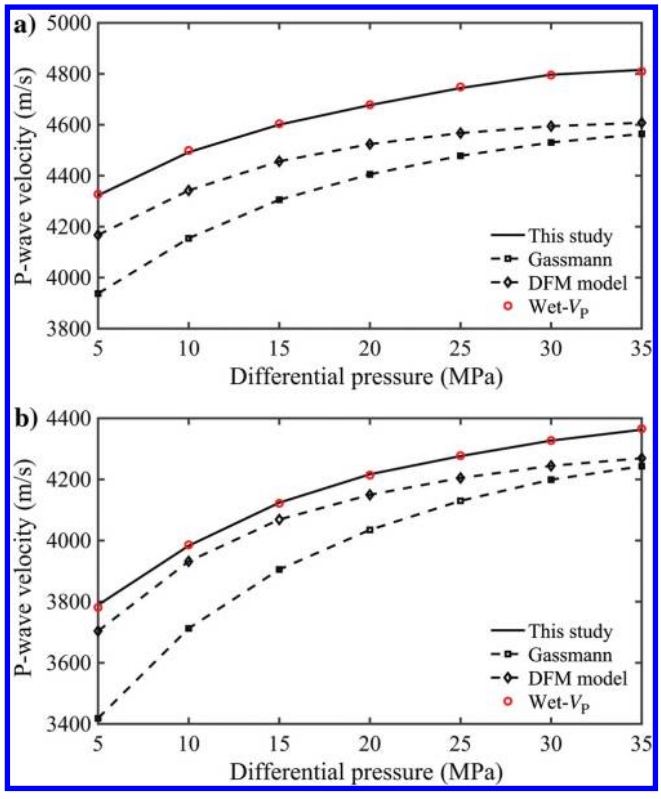

Figure 9. The P-wave velocities for the water-saturated tight sandstone samples (a) 1 and (b) 2 using Gassmann equation, the DFM model, and this study. The solid curves are predictions of our model, and the broken curves with diamonds and squares represent the predictions of the DFM model and Gassmann equation, whereas the red circles are measurements.

and this is because the LFF effect between the cracks and the pores is not considered in this theory. On the other hand, the results obtained with our model are in better in agreement with the experimental data than those of the other models.

CONCLUSION

We have derived new wave-propagation equations for cracked porous media by generalizing the Biot-Rayleigh theory, describing local-squirt flow attenuation, to the case of penny-shaped inclusions, which represent the cracks. The theory has as input parameters measurable properties such as the crack radius, density, and aspect ratio, which highly affect the anelastic properties of the rock. The crack radius mainly alters the relaxation frequency of the squirt-flow mechanism, but not the amount of dispersion and attenuation, which is highly affected by the crack density and aspect ratio. Moreover, our study shows that the cracks have a major effect on the seismic wave velocity, although their porosity is small. Variations in the crack density can cause significant velocity changes. Moreover, our model is consistent with Gassmann's theory and honors the experimental data of attenuation and velocity dispersion.

ACKNOWLEDGMENTS

This work is supported by the Cultivation Program of the "111" Project of China, Distinguished Professor Program of Jiangsu Province, China, the National Natural Science Foundation of China (no. 41704109), and the Fundamental Research Funds for the Central Universities, China.

DATA AND MATERIALS AVAILABILITY

Data associated with this research are available and can be obtained by contacting the corresponding author.

APPENDIX A

EXPRESSIONS OF THE STIFFNESS COEFFICIENTS

Following Ba et al. (2011), the stiffness coefficients can be given by

$$\lambda_c = (1-\phi)K_s - \frac{2}{3}\mu + \left(2 - \frac{K_s}{K_f}\right)(\phi_1\alpha_1 M_1 + \phi_2\alpha_2 M_2) - \left(1 - \frac{K_s}{K_f}\right)(\phi_1^2 M_1 + \phi_2^2 M_2), \tag{A-1}$$

$$\alpha_1 = \frac{\beta\phi_1 K_s}{\gamma K_f} + \phi_1, \qquad \alpha_2 = \frac{\phi_2 K_s}{\gamma K_f} + \phi_2 \tag{A-2}$$

$$M_1 = \frac{K_f}{\left(\frac{\beta}{\gamma} + 1\right)\phi_1}, \qquad M_2 = \frac{K_f}{\left(\frac{1}{\gamma} + 1\right)\phi_2}, \tag{A-3}$$

$$\gamma = \frac{K_s}{K_f}\left(\frac{\beta\phi_1 + \phi_2}{1 - \phi - \frac{K_b}{K_s}}\right) \tag{A-4}$$

$$\beta = \frac{\phi_{20}}{\phi_{10}}\left[\frac{1 - (1-\phi_{10})\frac{K_s}{K_{b1}}}{1 - (1-\phi_{20})\frac{K_s}{K_{b2}}}\right] \tag{A-5}$$

where K_s is the bulk modulus of the solid, K_{b1} and K_{b2} are the dry bulk moduli of host medium and inclusions, and K_b is the dry moduli of the solid.

APPENDIX B

KINETIC ENERGY AND DISSIPATION FUNCTION

Following Ba et al. (2011), the kinetic energy function is determined by

$$T = \frac{1}{2}(1-\phi)\rho_s \sum_i \dot{u}_i^2 + \frac{1}{2}\rho_f \sum_m \int_{\Omega_m} \sum_i (\dot{u}_i + \dot{w}_i^{(m)} + l^{(m)})^2 d\Omega_m. \tag{B-1}$$

Compared with spherical oscillations (Ba et al., 2011), the only difference is the microvelocity field of the LFF induced by periodic cylindrical oscillations. Hence, we only analyze the terms related with $l^{(m)}$ in the above integral. First, in the pore volume Ω_1, we have

$$\rho_f \int_{\Omega_1} \sum_i (\dot{u}_i l_i^{(1)}) d\Omega_1 = 0. \tag{B-2}$$

Due to the LFF in the radial direction and a symmetrical penny-shaped inclusion, the integral in equation B-2 is zero. In addition, we also have

$$\rho_f \int_{\Omega_1} \sum_i (w_i^{(1)} l_i^{(1)}) d\Omega_1 = 0. \tag{B-3}$$

Combining the above analysis, the kinetic energy function of LFF in the pore volume Ω_1 can be written as

$$T_{L,\text{out}} = \frac{1}{2}\rho_f \int_{\Omega_1} \sum_i (l_i^{(1)})^2 d\Omega_1. \tag{B-4}$$

The equation of the fluid-mass conservation can be generalized as

$$2\pi R h \dot{R} \phi_{20} = 2\pi r h \dot{r}_{\text{out}} \phi_{10}, \tag{B-5}$$

where $\dot{R}$ is the fluid particle velocity at the boundary between the two pore volumes $R < r \le R + L \le C$ and $\dot{r}_{\text{out}}$ is the fluid particle velocity outside the inclusion, where L is the characteristic fluid flow length, $L = (R_0^2/12)^{1/2}$ (Pride et al., 2004).

Hence, by substituting equation B-5 into equation B-4, we get

$$\begin{aligned} T_{L,\text{out}} &= \frac{1}{2}\rho_f \phi_{10} \int_R^{L+R} 2\pi r h \left(\frac{\phi_{20} R}{\phi_{10} r}\dot{R}\right)^2 dr \\ &= \rho_f \frac{\phi_{20}^2}{\phi_{10}} \pi h R^2 \dot{R}^2 \ln\frac{L+R}{R}. \end{aligned} \tag{B-6}$$

Second, in Ω_2 (inclusions), we have

$$\rho_f \int_{\Omega_2} \sum_i (\dot{u}_i l_i^{(2)}) d\Omega_2 = 0. \tag{B-7}$$

Because the directions of the global and LFF are radial, we can assume $w_i^{(2)} = l_i^{(2)}$ and have

$$\rho_f \int_{\Omega_2} \sum_i (w_i^{(2)} l_i^{(2)}) d\Omega_2 = \rho_f \int_{\Omega_2} \sum_i (l_i^{(2)})^2 d\Omega_2. \tag{B-8}$$

Combining these analyses, the kinetic energy function of LFF in Ω_2 can be written as

$$T_{L,\text{inter}} = \frac{3}{2}\rho_f \int_{\Omega_2} \sum_i (l_i^{(2)})^2 d\Omega_2. \tag{B-9}$$

The equation of the fluid-mass conservation is (Ba et al., 2014)

$$\frac{d\rho_f}{dt} + \rho_f \left(\frac{1}{r}\frac{\partial}{\partial r}(\dot{r}_{\text{in}})\right) = 0. \tag{B-10}$$

From this equation, we obtain the fluid particle velocity inside the inclusion:

$$\dot{r}_{\text{in}} = \frac{\dot{R}}{R} r, \tag{B-11}$$

where $0 < r \le R$.

Hence, by substituting equation B-11 into equation B-9, we obtain

$$T_{L,\text{inter}} = \frac{3}{2}\rho_f \phi_{20} \int_0^R 2\pi r h \left(\frac{\dot{R}}{R} r\right)^2 dr = \frac{3}{4}\rho_f \phi_{20} \pi h R^2 \dot{R}^2. \tag{B-12}$$

Here, we denote the volume fraction of inclusions per unit volume of composite as $v_2 = \pi R^2 h N_0$. By using this relation and $\phi_2 = v_2 \phi_{20}$, we obtain

$$R^2 = \frac{\phi_2}{\pi h N_0 \phi_{20}}. \tag{B-13}$$

From equation 2, we have

$$\dot{R} = \frac{1}{2}\phi_1 R_0 \dot{\varsigma}. \tag{B-14}$$

Combining equations B-13 and B-14 with equations B-6 and B-12 gives

$$\begin{aligned} T_{\text{LFF}} &= N_0 (T_{L,\text{inter}} + T_{L,\text{out}}) \\ &= \frac{3}{16}\rho_f \phi_1^2 \phi_2 R_0^2 \dot{\varsigma}^2 + \frac{1}{4}\rho_f \frac{\phi_1^2 \phi_2 \phi_{20}}{\phi_{10}} \ln\frac{L+R_0}{R_0} R_0^2 \dot{\varsigma}^2. \end{aligned} \tag{B-15}$$

In a similar way, the dissipation function of LFF in two pore volumes can be expressed as

$$\begin{aligned} D_{L,\text{out}} &= \frac{1}{2}\phi_{10}^2 \frac{\eta}{\kappa_1} \int_R^{L+R} 2\pi r h \left(\frac{\phi_{20} R}{\phi_{10} r}\dot{R}\right)^2 dr \\ &= \frac{\eta \phi_{20}^2}{\kappa_1} \pi h R^2 \dot{R}^2 \ln\frac{L+R}{R}. \end{aligned} \tag{B-16}$$

$$D_{L,\text{inter}} = \frac{3}{2}\phi_{20}^2 \frac{\eta}{\kappa_2} \int_0^R 2\pi r h \left(\frac{\dot{R}}{R} r\right)^2 dr = \frac{3}{4}\phi_{20}^2 \frac{\eta}{\kappa_2} \pi h R^2 \dot{R}^2. \tag{B-17}$$

Substituting equations B-5, B-11, B-13, and B-14 into equations B-16 and B-17 gives

$$D_{\mathrm{LFF}} = \frac{3}{16}\frac{\eta\phi_1^2\phi_{20}\phi_2}{\kappa_2}R_0^2\dot{\varsigma}^2 + \frac{1}{4}\frac{\eta\phi_1^2\phi_{20}\phi_2}{\kappa_1}\ln\frac{L+R_0}{R_0}R_0^2\dot{\varsigma}^2. \tag{B-18}$$

APPENDIX C

MAIN RESULTS OF THE TANG MODEL AND THE DFM MODEL

Tang et al. (2012) develop a unified elastic wave theory to model the effects of LFF between pores and cracks, where

$$K = K_b + \frac{\alpha^2}{\frac{(\alpha-\phi)}{K_s} + \frac{\phi}{K_f} + S(\omega)}, \tag{C-1}$$

where K is the saturated bulk modulus of the rock and α is the Biot coefficient. The term $S(\omega)$ governs the LFF, and it is given by

$$S(\omega) = \frac{\frac{8\varepsilon(1-v_0)(1+\lambda)^3}{3\mu_0}\left(\frac{\frac{1}{K_0}-\frac{1}{K_s}}{\frac{1}{K_b}-\frac{1}{K_0}}\right)M}{1-\frac{3i\omega\eta(1+2\lambda)}{2K_f\lambda\gamma^2}\left[1+\frac{4(1-v_0)K_f(1+\lambda)^3}{3\pi\mu_0\gamma(1+2\lambda)}M\right]}, \tag{C-2}$$

where $M = 1 + ((4-5v_0)/(2(7-5v_0)))((\lambda^3)/((1+\lambda)^3)) + (9/(2(7-5v_0)))((\lambda^5)/((1+\lambda)^5))$, $\lambda = ((3\phi_c)/(4\pi\varepsilon))^{\frac{1}{3}}$; μ_0, K_0, and v_0 are the shear modulus, bulk modulus, and Poisson's ratio of the background medium in the absence of squirt flow, crack density ε, and aspect ratio γ.

Yao et al. (2015) rederive and modify Tang's model as

$$K = K_b + \frac{\alpha^2}{\frac{(\alpha-\phi)}{K_s} + \frac{\phi}{K_f} - \Delta S(\omega)}, \tag{C-3}$$

where $\Delta S(\omega) = S(0) - S(\omega)$, $S(0) = (8\varepsilon(1-v_0)(1+\lambda)^3)/(3\mu_0)((1/K_0)-(1/K_s))/((1/K_b)-(1/K_0))M$.

APPENDIX D

EXPRESSIONS OF THE MORI-TANAKA MODEL

According to the Mori-Tanaka theory (Mori and Tanaka, 1973), the effective compliances are

$$\frac{1}{K_{\mathrm{stiff}}} = \frac{1}{K_s}\left(1 + \frac{\phi_{\mathrm{stiff}}}{1-\phi_{\mathrm{stiff}}}P\right), \tag{D-1}$$

$$\frac{1}{\mu_{\mathrm{stiff}}} = \frac{1}{\mu_s}\left(1 + \frac{\phi_{\mathrm{stiff}}}{1-\phi_{\mathrm{stiff}}}Q\right), \tag{D-2}$$

where K_{stiff} and μ_{stiff} are the bulk and shear moduli of the host material, respectively, ϕ_{stiff} is the stiff porosity, and P and Q are the normalized pore compressibility and shear compliance, respectively.

Cracks are introduced into the host material by using the Mori-Tanaka theory, and neglecting the interaction between cracks and pores. It results in the following effective compliances:

$$\frac{1}{K_{\mathrm{eff}}} = \frac{1}{K_{\mathrm{stiff}}}\left(1 + \frac{16(1-(v_{\mathrm{stiff}})^2)}{9(1-2v_{\mathrm{stiff}})}\varepsilon\right), \tag{D-3}$$

$$\frac{1}{G_{\mathrm{eff}}} = \frac{1}{G_{\mathrm{stiff}}}\left(1 + \frac{32(1-v_{\mathrm{stiff}})(5-v_{\mathrm{stiff}})}{45(2-v_{\mathrm{stiff}})}\varepsilon\right), \tag{D-4}$$

where $v_{\mathrm{stiff}} = (3K_{\mathrm{stiff}} - 2G_{\mathrm{stiff}})/(6K_{\mathrm{stiff}} + 2G_{\mathrm{stiff}})$ and crack density ε.

REFERENCES

Achenbach, J. D., 1984, Wave propagation in elastic solids: Elsevier.

Adam, L., and T. Otheim, 2013, Elastic laboratory measurements and modeling of saturated basalts: Journal of Geophysical Research: Solid Earth, **118**, 840–851, doi: 10.1002/jgrb.50090.

Ba, J., J. M. Carcione, and J. X. Nie, 2011, Biot-Rayleigh theory of wave propagation in double-porosity media: Journal of Geophysical Research: Solid Earth, **116**, B06202, doi: 10.1029/2010JB008185.

Ba, J., W. Xu, L. Y. Fu, J. M. Carcione, and L. Zhang, 2017, Rock anelasticity due to patchy saturation and fabric heterogeneity: A double double-porosity model of wave propagation: Journal of Geophysical Research: Solid Earth, **122**, 1949–1976, doi: 10.1002/2016JB013882.

Ba, J., L. Zhang, W. Sun, and Z. Hao, 2014, Velocity field of wave-induced local fluid flow in double-porosity media: Science China Physics, Mechanics and Astronomy, **57**, 1020–1030, doi: 10.1007/s11433-014-5442-0.

Ba, J., L. Zhang, D. Wang, Z. Yuan, W. Cheng, R. Ma, and C. F. Wu, 2018, Experimental analysis on P-wave attenuation in carbonate rocks and reservoir identification: Journal of Seismic Exploration, **27**, 371–402.

Ba, J., J. Zhao, J. M. Carcione, and X. Huang, 2016, Compressional wave dispersion due to rock matrix stiffening by clay squirt flow: Geophysical Research Letters, **43**, 6186–6195, doi: 10.1002/2016GL069312.

Berryman, J. G., 1980, Long wavelength propagation in composite elastic media. 2. Ellipsoidal inclusions: The Journal of the Acoustical Society of America, **68**, 1820–1831, doi: 10.1190/1.1440450.

Berryman, J. G., 2007, Seismic waves in rocks with fluids and fractures: Geophysical Journal International, **171**, 954–974, doi: 10.1111/j.1365-246X.2007.03563.x.

Berryman, J. G., and H. F. Wang, 1995, The elastic coefficients of double-porosity models for fluid transport in jointed rock: Journal of Geophysical Research: Solid Earth, **100**, 24611–24627, doi: 10.1029/95JB02161.

Biot, M. A., 1956, Theory of propagation of elastic waves in fluid-saturated porous solid — Part 1: Low frequency range: Journal of the Acoustical Society of America, **28**, 168–178, doi: 10.1121/1.1908239.

Biot, M. A., 1962, Mechanics of deformation and acoustic propagation in porous media: Journal of Applied Physics, **33**, 1482–1498, doi: 10.1063/1.1728759.

~~Carcione, J. M., 2014, Wave fields in real media. Theory and numerical simulation of wave propagation, Anisotropic, anelastic, porous and electromagnetic media, 3rd ed.: Elsevier.~~

Carcione, J. M., and B. Gurevich, 2011, Differential form and numerical implementation of Biot's poroelasticity equations with squirt dissipation: Geophysics, **76**, no. 6, N55–N64, doi: 10.1190/geo2010-0169.1.

Chapman, M., 2001, Modelling the wide-band laboratory response of rock samples to fluid and pressure changes: Ph.D. thesis, University of Edinburgh.

Chapman, M., 2003, Frequency-dependent anisotropy due to meso-scale fractures in the presence of equant porosity: Geophysical Prospecting, **51**, 369–379, doi: 10.1046/j.1365-2478.2003.00384.x.

Chapman, M., S. V. Zatsepin, and S. Crampin, 2002, Derivation of a microstructural poroelastic model: Geophysical Journal International, **151**, 427–451, doi: 10.1046/j.1365-246X.2002.01769.x.

Cheng, C. H., and M. N. Toksöz, 1979, Inversion of seismic velocities for the pore aspect ratio spectrum of a rock: Journal of Geophysical Research: Solid Earth, **84**, 7533–7543, doi: 10.1029/JB084iB13p07533.

David, E. C., and R. W. Zimmerman, 2011, Compressibility and shear compliance of spheroidal pores: Exact derivation via the Eshelby tensor, and asymptotic expressions in limiting cases: International Journal of Solids and Structures, **48**, 680–686, doi: 10.1016/j.ijsolstr.2010.11.001.

David, E. C., and R. W. Zimmerman, 2012, Pore structure model for elastic wave velocities in fluid-saturated sandstones: Journal of Geophysical Research: Solid Earth, **117**, B07210, doi: 10.1029/2012JB009195.

Dunn, K. J., 1986, Acoustic attenuation in fluid-saturated porous cylinders at low frequencies: The Journal of the Acoustical Society of America, **79**, 1709–1721, doi: 10.1121/1.393232.

Dvorkin, J., and A. Nur, 1993, Dynamic poroelasticity: A unified model with the squirt and the Biot mechanisms: Geophysics, **58**, 524–533, doi: 10.1190/1.1443435.

Endres, A. L., and R. J. Knight, 1997, Incorporating pore geometry and fluid pressure communication into modeling the elastic behavior of porous rocks: Geophysics, **62**, 106–117, doi: 10.1190/1.1444110.

Eshelby, J. D., 1957, The determination of the elastic field of an ellipsoidal inclusion, and related problems: Proceedings of the Royal Society of London, Series A, **241**, 376–396, doi: 10.1098/rspa.1957.0133.

Fortin, J., Y. Guéguen, and A. Schubnel, 2007, Effects of pore collapse and grain crushing on ultrasonic velocities and V_p/V_s: Journal of Geophysical Research: Solid Earth, **112**, B08207, doi: 10.1029/2005JB004005.

Galvin, R. J., and B. Gurevich, 2009, Effective properties of a poroelastic medium containing a distribution of aligned cracks: Journal of Geophysical Research: Solid Earth, **114**, B7, doi: 10.1029/2008JB006032.

Gassmann, F., 1951, Über die Elastizität poröser Medien: Vierteljahrsschriftder Naturforschenden Gesellschaft in Zürich, **96**, 1–23.

Guo, J., J. Germán Rubino, N. D. Barbosa, S. Glubokovskikh, and B. Gurevich, 2018a, Seismic dispersion and attenuation in saturated porous rocks with aligned fractures of finite thickness: Theory and numerical simulations — Part 1: P-wave perpendicular to the fracture plane: Geophysics, **83**, no. 1, WA49–WA62, doi: 10.1190/geo2017–0065.1.

Guo, J., J. Germán Rubino, N. D. Barbosa, S. Glubokovskikh, and B. Gurevich, 2018b, Seismic dispersion and attenuation in saturated porous rocks with aligned fractures of finite thickness: Theory and numerical simulations — Part 2: Frequency-dependent anisotropy: Geophysics, **83**, no. 1, WA63–WA71, doi: 10.1190/geo2017-0066.1.

Guo, J., J. G. Rubino, S. Glubokovskikh, and B. Gurevich, 2017, Effects of fracture intersections on seismic dispersion: Theoretical predictions versus numerical simulations: Geophysical Prospecting, **65**, 1264–1276, doi: 10.1111/1365-2478.12474.

Gurevich, B., M. Brajanovski, R. J. Galvin, T. M. Müller, and J. Toms-Stewart, 2009b, P-wave dispersion and attenuation in fractured and porous reservoirs — Poroelasticity approach: Geophysical Prospecting, **57**, 225–237, doi: 10.1111/j.1365-2478.2009.00785.x.

Gurevich, B., D. Makarynska, O. B. de Paula, and M. Pervukhina, 2010, A simple model for squirt-flow dispersion and attenuation in fluid-saturated granular rocks: Geophysics, **75**, no. 6, N109–N120, doi: 10.1190/1.3509782.

Gurevich, B., D. Makarynska, and M. Pervukhina, 2009a, Are penny-shaped cracks a good model for compliant porosity?: 79th Annual International Meeting, SEG, Expanded Abstracts, 3431–3435, doi: 10.1190/1.3255575.

Hudson, J. A., E. Liu, and S. Crampin, 1996, The mechanical properties of materials with interconnected cracks and pores: Geophysical Journal International, **124**, 105–112, doi: 10.1111/j.1365-246X.1996.tb06355.x.

Jakobsen, M., J. A. Hudson, and T. A. Johansen, 2003, T-matrix approach to shale acoustics: Geophysical Journal International, **154**, 533–558, doi: 10.1046/j.1365-246X.2003.01977.x.

Khalid, P., and N. Ahmed, 2016, Modulus defect, velocity dispersion and attenuation in partially-saturated reservoirs of Jurassic sandstone, Indus basin, Pakistan: Studia Geophysica et Geodaetica, **60**, 112–129, doi: 10.1007/s11200-015-0804-2.

Kuster, G. T., and M. N. Toksöz, 1974, Velocity and attenuation of seismic waves in two phase media: Geophysics, **39**, 587–618, doi: 10.1190/1.1440450.

Mavko, G., and A. Nur, 1975, Melt squirt in the aesthenosphere: Journal of Geophysical Research, **80**, 1444–1448, doi: 10.1029/JB080i011p01444.

Mori, T., and K. Tanaka, 1973, Average stress in matrix and average elastic energy of materials with misfitting inclusions: Acta Metallurgica, **21**, 571–574, doi: 10.1016/0001-6160(73)90064-3.

Müller, T. M., B. Gurevich, and M. Lebedev, 2010, Seismic wave attenuation and dispersion resulting from wave-induced flow in porous rocks — A review: Geophysics, **75**, no. 5, A147–A164, doi: 10.1190/1.3463417.

Murphy, W. F., III, K. W. Winkler, and R. L. Kleinberg, 1986, Acoustic relaxation in sedimentary rocks, dependence on grain contacts and fluid saturation: Geophysics, **51**, 757–766, doi: 10.1190/1.1442128.

Norris, A. N., 1985, A differential scheme for the effective moduli of composites: Mechanics of Materials, **4**, 1–16, doi: 10.1016/0167-6636(85)90002-X.

Pride, S. R., and J. G. Berryman, 2003, Linear dynamics of double-porosity and dual-permeability materials — Part 1: Governing equations and acoustic attenuation: Physical Review E, **68**, 036603, doi: 10.1103/PhysRevE.68.036603.

Pride, S. R., J. G. Berryman, and J. M. Harris, 2004, Seismic attenuation due to wave induced flow: Journal of Geophysical Research, **109**, B01201, doi: 10.1029/2003JB002639.

Quintal, B., S. M. Schmalholz, and Y. Y. Podladchikov, 2011, Impact of fluid saturation on the reflection coefficient of a poroelastic layer: Geophysics, **76**, no. 2, N1–N12, doi: 10.1190/1.3553002.

Rayleigh, L., 1917, On the pressure developed in a liquid during the collapse of a spherical cavity: Philosophical Magazine, **34**, 94–98, doi: 10.1080/14786440808635681.

Shapiro, S. A., 2003, Elastic piezo sensitivity of porous and fractured rocks: Geophysics, **68**, 482–486, doi: 10.1190/1.1567215.

Song, Y., H. Hu, and J. W. Rudnicki, 2016, Deriving Biot-Gassmann relationship by inclusion-based method: Geophysics, **81**, no. 6, D657–D667, doi: 10.1190/geo2015-0432.1.

Tang, X., 2011, A unified theory for elastic wave propagation through porous media containing cracks — An extension of Biot's poroelastic wave theory: Science China-Earth Sciences, **54**, 1441–1452, doi: 10.1007/s11430-011-4245-7.

Tang, X. M., X. L. Chen, and X. K. Xu, 2012, A cracked porous medium elastic wave theory and its application to interpreting acoustic data from tight formations: Geophysics, **77**, no. 6, D245–D252, doi: 10.1190/geo2012-0091.1.

Thomsen, L., 1985, Biot-consistent elastic moduli of porous rocks: Low-frequency limit: Geophysics, **50**, 2797–2807, doi: 10.1190/1.1441900.

Tran, D. T., C. S. Rai, and C. H. Sondergeld, 2008, Changes in crack aspect-ratio concentration from heat treatment: A comparison between velocity inversion and experimental data: Geophysics, **73**, no. 4, E123–E132, doi: 10.1190/1.2928848.

Walsh, J. B., 1965, The effect of cracks on the compressibility of rock: Journal of Geophysical Research, **70**, 381–389, doi: 10.1029/JZ070i002p00381.

Wang, Y., C. H. Li, and Y. Z. Hu, 2018, Experimental investigation on the fracture behavior of Black Shale by acoustic emission monitoring and CT image analysis during uniaxial compression: Geophysical Journal International, **213**, 660–675, doi: 10.1093/gji/ggy011/4810549.

Yao, Q., D. H. Han, F. Yan, and L. Zhao, 2015, Modeling attenuation and dispersion in porous heterogeneous rocks with dynamic fluid modulus: Geophysics, **80**, no. 3, D183–D194, doi: 10.1190/geo2013-0410.1.

Yin, S., D. Lv, and W. Ding, 2018, New method for assessing micro fracture stress sensitivity in tight sandstone reservoirs based on acoustic experiments: International Journal of Geomechanics, **18**, 04018008, doi: 10.1061/(ASCE)GM.1943-5622.0001100.

Zheng, P., B. Ding, and X. Sun, 2017, Elastic wave attenuation and dispersion induced by mesoscopic flow in double-porosity rocks: International Journal of Rock Mechanics and Mining Sciences, **91**, 104–111, doi: 10.1016/j.ijrmms.2016.11.018.